WEIGHTED-TYPE IMAGE SEGMENTATION MODEL VIA COUPLING HEAT KERNEL CONVOLUTION WITH HIGH-ORDER TOTAL VARIATION

MENGXIAO GENG[1], LIN YANG[1], ZHI-FENG PANG[1,*], HAOHUI ZHU[2]

[1]*Department of Mathematics, Henan University, Kaifeng 475004, China*
[2]*Department of Ultrasound, Henan Provincial People's Hospital, Zhengzhou 450003, China*

Abstract. Image segmentation is an essential step for many applications in the field of the image analysis. One of the main challenges for this task is how to accurately locate complicated boundary and properly segment a region of interest efficiently. To this end, this paper provides a new scheme by combining the adaptive weight function and the high-order total variation term to improve the robustness of the classical active contour model. In order to reduce the computational complexity, our model uses the heat kernel convolution with adaptive weight to approximate the perimeter of the segmentation area. Due to the nonsmoothness of the proposed model, we adopt the alternating direction method of multipliers to solve it. Numerical implementations on several different types of images illustrate that our proposed scheme demonstrates better segmentation performance and robustness than several existing state-of-the-art segmentation models.

Keywords. Adaptive weight function; Active contour model; High order total variation; Heat kernel convolution; Image segmentation.

1. INTRODUCTION

Image segmentation is one of the most important techniques for detecting objects and analyzing images in the field of computer vision. In recent decades, it has been widely used in remote sensing, medical image processing, target tracking, document image processing, and fingerprint identification [1, 2, 3, 4, 5]. In general, the aim of the image segmentation is to divide the image into several disjoint regions according to the characteristics of gray, color, spatial texture, and geometric shape. In the same region, these features demonstrate consistency or similarity, but, in the different regions, these features demonstrate the obvious differences. However, due to the interference of image degradation information [6, 7, 8, 9], the image segmentation is still a challenge in some practical applications. For solving various application scenarios, the segmentation model can be divided into data-driven models [10, 11, 12, 13, 14] and model-driven models [15, 16, 17, 18]. Data-driven models usually require a large amount of image data and strong model-based supports [10, 11, 12, 13, 14]. However, many difficulties, such as insufficient data, background noise, local intensity variations, and complex segmentation targets,

---

make the segmentation problem quite challenging. Especially, data-driven models are mostly black boxes without rigorous mathematical justification and can be very difficult to interpret. Model-driven models can overcome some problems, such as limited available data and imperfect models. Among the model-driven models, active contour models have been widely concerned, which predefines an energy functional with the intensity and the gradient information based on the intrinsic properties of images.

To the active contour models, the Chan-Vese (CV) model [19] has been successfully used in the two-phase segmentation with the assumption that each image region is statistically homogeneous and then implemented by using the Level Set Method (LSM). However, its nonconvexity leads the segmentation results completely depending on the original contour for the numerical implementation. To this end, Chan et al. [20] established a convex relaxation strategy and proved its equivalence and theoretical consistency with the CV model. Since the convex relaxation form corresponds to a non-smooth optimization problem, it can be solved by some fast operator splitting algorithms and it can also avoid the defect of the LSM in the distance function requiring periodic reinitialization of the active contour. As an improvement of the convex relaxation strategy, Pock et al. [21] considered to calculate the partition problem of the minimum perimeter based on the Potts model and then used the primal dual algorithm to solve it quickly. In addition, based on the graph cut technology, Yuan et al. [22] proposed a continuous maximum flow and minimum cut model constrained by prior supervised information and applied it to interactive image segmentation.

Above models were mainly applied to segment the piecewise constant image. In order to segment the intensity inhomogeneity image, Li et al. [23] proposed a region-extensible fitting model by introducing some local statistical information based on the CV model. This model mainly used the Gaussian kernel on the fidelity term to describe the intensity inhomogeneity and then overcome the limitation of the CV model but is unsuitable to the high noise image. To this end, Wang et al. [24] used the mean filter to provide images with the higher contrast and then proposed a local CV model (LCV). Furthermore, Zhang et al. [25] proposed to model non-uniform targets as the Gaussian distributions with different mean values and variances and used moving windows to map the original image to another domain. However, above models still have numerical difficulties such as the high computational complexity and the tuning of more parameters.

Recently, the feature function representing the curve evolution method in the segmentation problem has been concerned. For example, the edge-weighted centoidal voronoi tessellation (EWCVT) models [26, 27] were tried to add a boundary length regularization to the k-means algorithm, which was then approximated by counting the dissimilar indices within local circles. Especially, Merriman, Bence, and Osher (MBO) [28] proposed to model and simulate the motion by the mean curvature, and to characterize the characteristic function of the inner region of the iterative diffusion curve through a threshold. The paper [29] further interpreted the MBO model as the characteristic function of Lyapunov functional minimization motion, so this model can be extended to the multiphase mean curvature motion problem with an arbitrary surface tension. In particular, the MBO model has been widely applied to region-based active contour segmentation due to its unique simplicity and unconditional stability [30]. In the convex relaxation model of the segmentation problem, the perimeter of the segmented region can be approximated as a feature function by the heat kernel convolution, so it can be quickly

solved by using an Iterative Convolutional Thresholding Method (ICTM) [16, 30], which is experimentally shown to be simple, efficient, and applicable to a wide range of region based segmentation problems.

Motivated by the active contour model and the ICTM, this paper proposes a new weighed active contour models by combining the heat kernel convolution and the high-order total variation regularization. In the established model, the curvature weight function is used to characterize the structural features of the image and the perimeter of the segmentation curve is approximated by the heat kernel convolution. At the same time, the higher-order total variation term describes some information inside the segmented region. In addition, the proposed model is an optimization problem containing separable operators, so we adopt the Alternating Direction Multiplier Method (ADMM) to solve it efficiently. The effectiveness of the model and algorithm can be verified by several selected natural and ultrasound image segmentation experiments. The experiment shows that the proposed model can not only improve the accuracy of image segmentation, but also improve the segmentation efficiency.

The rest of the paper is organized as follows. We review some classical active contour models in Section 2. Then we propose a weighted type image segmentation model coupling thermal kernel convolution and higher-order total variation regularization in Section 3. We introduces the numerical algorithm based on the ADMM and simultaneously give the corresponding solution. In Section 4, some numerical comparisons are arranged to illustrate the efficiency of the proposed model. Finally, we report our conclusion in Section 5, the last section.

2. RELATED WORKS

Let $\Omega \subset \mathbb{R}^2$ be a bounded open connected set, Γ be a compact curve in Ω, and $f : \Omega \to \mathbb{R}$ be a given image. The segmentation problem is to partition the image domain into several disjoint subdomain. This section provides an overview of existing segmentation approaches that are closely related to our proposed model.

2.1. **CV model.** Mumford-Shah Model [31] is the most worthy of a class of active contour models, which can be simplified into the Chan-Vese (CV) model [19] as follows

$$\min_{\Gamma, c_1, c_2} \frac{\lambda}{2} \int_{\Omega} (f - c_1)^2 \mathrm{d}x + \frac{\lambda}{2} \int_{\Omega \setminus \Omega_c} (f - c_2)^2 \mathrm{d}x + L(\Gamma),$$

where $c_1, c_2 \in \mathbb{R}$ are the average values of the pixels inside and outside Γ for the two-phase segmentation, $L(\Gamma)$ is the length of the curve Γ, λ is the positive parameters, and Ω_c is a closed subset of the image f. The CV model is a representative model based on the regional information. Its numerical implementation uses the LSM, which is convenient for handling topological changes, dividing more complex objects, and realizing the expansion from low-dimensional to high-dimensional. However, in order to maintain the nature of the distance function, it is necessary to reconstruct the level set function every other period of time and then causes higher time-consuming.

2.2. **GMAC model.** In order to avoid the disadvantage of periodically reinitializing the active contour when using the LSM, Bresson et al. [32] proposed a Global Minimizer of Active Contour (GMAC) by solving the following optimization problem

$$\min_{u \in [0,1]} \lambda \int_{\Omega} \left((f - c_1)^2 - (f - c_2)^2 \right) u \mathrm{d}x + \int_{\Omega} g(f) |\nabla u| \mathrm{d}x,$$

where $|\nabla u| = \sqrt{u_{x_1}^2 + u_{x_2}^2}$, c_1, c_2 and the edge detection function $g(f)$ can be obtained by

$$c_1 := c_1(u) = \frac{\int_\Omega f u \mathrm{dx}}{\int_\Omega u \mathrm{dx}}, \ c_2 := c_2(u) = \frac{\int_\Omega f(1-u)\mathrm{dx}}{\int_\Omega (1-u)\mathrm{dx}} \text{ and } g(f) = \frac{1}{1+\gamma|\nabla f|^2}. \tag{2.1}$$

Here γ is a positive parameter and $|\nabla f| = \sqrt{f_{x_1}^2 + f_{x_2}^2}$. The GMAC model can determine the global minimum of energy and is not sensitive to the selection of the initial contour.

2.3. ICTM model.

In [33], Wang et al. proposed a novel Iterative Convolution-Thresholding Method (ICTM) in which the length term is approximated by a functional of characteristic functions in terms of the heat kernel convolution as

$$\min_{u \in \{0,1\}} \lambda \int_\Omega ((f-c_1)^2 - (f-c_2)^2)u\mathrm{dx} + \sqrt{\frac{\pi}{\tau}} \int_\Omega uG_\tau * (1-u)\mathrm{dx}, \tag{2.2}$$

where $G_\tau(\mathrm{x}) = \frac{1}{4\pi\tau}\exp\left(-\frac{\|\mathrm{x}\|^2}{4\tau}\right)$ is a Gaussian kernel with the standard derivation τ, $*$ is the convolution operator, c_1 and c_2 can be obtained from (2.1). In the ICTM, the interface between two different segment domains is implicitly represented by their characteristic function. To the model (2.2), the authors in [33] designed an iterative convolution thresholding method to minimize the approximate energy. This method has the obvious advantages of simplicity, easy implementation and strong robustness.

2.4. DTC model.

Since the curvature regularity can provide strong priors on edge continuity, it has been widely concerned in the field of the image segmentation. Recently, Zhong et al. [34] proposed a discrete total curvature (DTC) by minimizing the normal curvatures along eight different directions as

$$\min_u \lambda \int_\Omega ((f-c_1)^2 - (f-c_2)^2)u\mathrm{dx} + \int_\Omega \psi(\kappa)|\nabla u|\mathrm{dx},$$

where $\psi(\kappa)$ is some appropriate functions of curvature, e.g.,

$$\psi(\kappa) = \begin{cases} 1 + \alpha|\kappa|, & \text{Total Absolute Curvature,} \\ \sqrt{1 + \alpha|\kappa|^2}, & \text{Total Roto-translation Variation,} \\ 1 + \alpha|\kappa|^2, & \text{Total Squared Curvature,} \end{cases}$$

and α is a positive constant. The curvature of the level lines is set as $\kappa \approx \sum_{\ell=1}^{8} |\kappa_\ell|$. Among them, we use the following definitions as

$$\kappa_\ell \approx \begin{cases} \dfrac{2d_\ell}{(p_\ell^\triangle - u_{i,j})^2 + h^2}, & \ell = 1,2,3,4, \\ \dfrac{2d_\ell}{(p_\ell^\square - u_{i,j})^2 + 2h^2}, & \ell = 5,6,7,8, \end{cases}$$

Here $p^\triangle$ and $p^\square$ are the intensity of the half point to the grid line and the center of every grid region in nine neighbourhoods, h is the grid size, and d_ℓ is the projection distance.

2.5. **WBHV model.** To describe the edge of the segmentation image, Yang et al. [35] recently based on the GMAC proposed to couple the weighted bounded Hessian variation regularization (WBHV) with the weighted total variation regularization as

$$\min_{u \in [0,1]} \int_\Omega \alpha(f)|\nabla u|\mathrm{dx} + \int_\Omega \beta(f)|\nabla^2 u|\mathrm{dx} + \lambda \int_\Omega (f-c_1)^2 u + (f-c_2)^2 (1-u)\mathrm{dx}, \qquad (2.3)$$

where $|\nabla^2 u| = \sqrt{u_{x_1 x_1}^2 + u_{x_1 x_2}^2 + u_{x_2 x_1}^2 + u_{x_2 x_2}^2}$, the weight functions $\alpha(f)$ and $\beta(f)$ are defined by

$$\alpha(f) = \left| \nabla \frac{1}{\sqrt{1+|\nabla f|^2}} \right| \text{ and } \beta(f) = \frac{1}{\sqrt{1+|\nabla f|^2}}. \qquad (2.4)$$

In model (2.3), the first term characterizes the length of the segmented region and the second term characterizes the smooth feature of the image feature function. Here, $\alpha(f)$ is used as the adaptive weight of first-order regularization to enhance the boundary at the edge. $\beta(f)$ is the adaptive weight of second-order regularization, which automatically stops at the edge and can smooth some unnecessary details. These two adaptive weights capture the boundary information more fully, and save the trouble of manually adjusting the parameters.

3. THE PROPOSED SCHEME

To the image segmentation problem, the effectiveness depends on not only the accurate description of the segmentation region but also the numerical method. For the WBHV (2.3), although there is a higher segmentation accuracy, it has higher computational complexity due to the non-smooth terms. A type of way to reduce computing complexity is to replace the non-smooth term by some approximation strategies. To this end, we combine the WBHV (2.3) with the approximation strategy used in the ICTM (2.2) and then consider the following modified model

$$\min_{u \in \{0,1\}, c_1, c_2} \sqrt{\frac{\pi}{\tau}} \int_\Omega \alpha(f)uG_\tau * (1-u)\mathrm{dx} + \int_\Omega \beta(f)|\nabla^2 u|\mathrm{dx} + \lambda \int_\Omega (f-c_1)^2 u + (f-c_2)^2 (1-u)\mathrm{dx}, \qquad (3.1)$$

where c_1 and c_2 can be obtain by the equation (2.1), and $\alpha(f)$ and $\beta(f)$ are defined in (2.4). Below, we discuss how to solve the u-subproblem.

Model (3.1) is a non-smooth due to the second term and also the binary optimization problem, so we need to employ some operator splitting schemes to decouple the Hessian operator from the Frobenius norm and also use the convex relaxed scheme to set $u \in [0, 1]$. To this end, we first introduce an auxiliary variable $\mathbf{z}$ and then equivalently transform problem (3.1) into the following constrained optimization problem

$$\begin{cases} \min_{\mathbf{z}, u \in [0,1]} \sqrt{\frac{\pi}{\tau}} \int_\Omega \alpha(f)uG_\tau * (1-u)\mathrm{dx} + \int_\Omega \beta(f)|\mathbf{z}|\mathrm{dx} \\ \qquad\qquad + \lambda \int_\Omega (f-c_1)^2 u + (f-c_2)^2 (1-u)\mathrm{dx}, \\ \text{s.t. } \mathbf{z} = \nabla^2 u. \end{cases} \qquad (3.2)$$

Based on the augmented Lagrangian method, problem (3.2) can be written as the following saddle point problem

$$\min_{\mathbf{z},u\in[0,1]} \max_{\boldsymbol{\eta}} \mathscr{L}(u,\mathbf{z},\boldsymbol{\eta}),$$

where

$$
\begin{aligned}
&\mathscr{L}(u,\mathbf{z},\boldsymbol{\eta})\\
&= \sqrt{\frac{\pi}{\tau}} \int_{\Omega} \alpha(f)uG_\tau * (1-u)\mathrm{d}x + \int_{\Omega} \beta(f)|\mathbf{z}|\,\mathrm{d}x + \lambda \int_{\Omega} (f-c_1)^2 u + (f-c_2)^2(1-u)\mathrm{d}x\\
&\quad + \langle \boldsymbol{\eta}, \mathbf{z} - \nabla^2 u \rangle + \frac{r}{2} \int_{\Omega} |\mathbf{z} - \nabla^2 u|^2 \mathrm{d}x,
\end{aligned}
$$

and the dual variable $\boldsymbol{\eta}$ is called the Lagrangian multiplier, and r is the penalty parameter. Note that it is usually hard to minimize the augmented Lagrangian function $\mathscr{L}(u,\mathbf{z},\boldsymbol{\eta})$ with respect to u and $\mathbf{z}$ simultaneously. However, if we minimize the augmented Lagrangian function with respect to u and $\mathbf{z}$ alternatively, we obtain two subproblems in each iteration and both of them are relatively easy to be solved by the alternating direction multiplier method (ADMM) as follows

$$
\begin{cases}
u^{k+1} = \underset{u\in[0,1]}{\mathrm{argmin}}\, \mathscr{L}\left(u,\mathbf{z}^k,\boldsymbol{\eta}^k\right), & (3.3)\\[2mm]
\mathbf{z}^{k+1} = \underset{\mathbf{z}}{\mathrm{argmin}}\, \mathscr{L}\left(u^{k+1},\mathbf{z},\boldsymbol{\eta}^k\right), & (3.4)\\[2mm]
\boldsymbol{\eta}^{k+1} = \boldsymbol{\eta}^k + r\left(\mathbf{z}^{k+1} - \nabla^2 u^{k+1}\right). & (3.5)
\end{cases}
$$

Now we mainly consider how to solve subproblems (3.3) and (3.4).

- To subproblem (3.3), it is a non-convex optimization problem due to the first term. To deal with this drawback, we linearize the objective function $\mathscr{L}\left(u,\mathbf{z}^k,\boldsymbol{\eta}^k\right)$ at the iteration u^k and then subproblem (3.3) can be approximately rewritten as

$$u^{k+1} = \underset{u\in[0,1]}{\mathrm{argmin}} \int_{\Omega} u\phi\left(u^k\right)\mathrm{d}x, \tag{3.6}$$

where

$$\phi\left(u^k\right) = \alpha(f)\sqrt{\frac{\pi}{\tau}}G_\tau * \left(1-2u^k\right) + \lambda\left((f-c_1)^2 - (f-c_2)^2\right) + r\,\mathrm{div}^2\left(\nabla^2 u^k - \mathbf{z}^k - \frac{\boldsymbol{\eta}^k}{r}\right).$$

It is obvious that solution u^{k+1} satisfies that

$$u^{k+1} = \begin{cases} 1, & \text{if } \phi\left(u^k\right) \le 0;\\ 0, & \text{otherwise.} \end{cases} \tag{3.7}$$

- To subproblem (3.4), it can be rewritten as

$$\min_{\mathbf{z}} \int_{\Omega} \beta(f)|\mathbf{z}|\mathrm{d}x + \frac{r}{2}\left\|\mathbf{z} - \left(\nabla^2 u^{k+1} - \frac{\boldsymbol{\eta}^k}{r}\right)\right\|_{\mathrm{F}}^2, \tag{3.8}$$

which is the classic $L^1 - L^2$ problem. So the closed form solution can be obtained by

$$\mathbf{z}^{k+1} = \max\left\{\left\|\nabla^2 u^{k+1} - \frac{\boldsymbol{\eta}^k}{r}\right\|_{\mathrm{F}} - \frac{\beta(f)}{r}, 0\right\} \frac{\nabla^2 u^{k+1} - \frac{\boldsymbol{\eta}^k}{r}}{\left\|\nabla^2 u^{k+1} - \frac{\boldsymbol{\eta}^k}{r}\right\|_{\mathrm{F}}}. \tag{3.9}$$

To sum up, the image segmentation algorithm based on the model (3.1) is described as follows.

Algorithm 1 Image Segmentation Algorithm Based on the Model (3.1)

1: **Input:** original image I, parameters λ, $\tau > 0$, r, maximum iteration $K_{\max}$, and stopping threshold ε;
2: **Initialize:** $u^0, \mathbf{z}^0 = \boldsymbol{\eta}^0 = 0$, set $k = 0$;
3: **while** (not converged and $k \leq K_{\max}$) **do**
4:   Compute $c_1(u^k), c_2(u^k)$ according to (2.1);
5:   Compute u^{k+1} with fixed $\mathbf{z}^k, \boldsymbol{\eta}^k$ according to (3.7);
6:   Compute $\mathbf{z}^{k+1}$ with fixed $u^{k+1}, \boldsymbol{\eta}^k$ according to (3.9);
7:   Update $\boldsymbol{\eta}^{k+1}$ according to (3.5);
8:   Check the convergence condition: $\left\| u^{k+1} - u^k \right\|_1 \leq \varepsilon \left\| u^k \right\|_1$;
9: **end while**

---

4. Numerical Experiments

To validate the effectiveness and robustness of the proposed scheme compared with other related models such as the CV [19], the GMAC [32], the ICTM [30], the WBHV [35], and the DTC [34], we perform several testings on some natural and ultrasound images. To the models and the corresponding numerical methods, there are several parameters to be tuned. To the stopping parameters, we choose the max number of outer iteration $I_{max} = 500$ and $\varepsilon = 10^{-3}$ for the above-mentioned models. In particular, experiments show that good segmentation results can be obtained when the maximum number of inner iterations K_{max} is 1. To other parameters, we carefully tune them to find the main parameters by the trial-and-error method in order to obtain the satisfied segmentation image. For more convenience, we set these main parameters in the models (CV; GMAC; ICTM; WBHV; DTC; OURS) to be the vector in terms of (λ; γ, λ; λ, τ; λ, r_3; λ, α; λ), where ';' is the separation mark. For the remaining parameters, we set $r = 0.2$, $\tau = 0.001$ for the gray images, $r = 0.6$, $\tau = 0.002$ for the color images in Algorithm 1, and $r_1 = 1$, $r_2 = 2$ in the WBHV. All the numerical experiments are performed via MATLAB (R2020a) on windows 10 (64bit) laptop computer with an Intel Core(TM)i5 7200UCPU 2.50GHz processor.

Beside of the parameters, some indexes are needed to measure the accuracy of the segmentation. Here we employ the following indexes such as segmentation accuracy (SA), F1-Score (F1), κ-coefficient (κ), and Jaccard Similarity (JS) [35], which are defined by

$$SA = \frac{TP + TN}{TP + TN + FP + FN}, \quad F1 = \frac{2PR}{P + R}, \quad \kappa = \frac{SA - M}{1 - M}, \quad \text{and} \quad JS = \frac{|S_1 \cap S_2|}{|S_1 \cup S_2|},$$

where TP (True Positive) and TN (True Negative) represent the correctly segmented and unsegmented regions, FP (False Positive) and FN (False Negative) represent the detected and undetected false-regions respectively. Here S_1 is the region by the Algorithm 1 and S_2 is the corresponding region of the ground truth. In addition, the parameters P, R and M used in F1 and κ are defined by

$$P = \frac{TP}{TP + FP}, \quad R = \frac{TP}{TP + FN} \quad \text{and} \quad M = \frac{(TP+FN)(TP+FP) + (FP+TN)(FN+TN)}{(TP+TN+FP+FN)^2}.$$

It is obvious if the values for these metrics are close to 1, the obtained segmentation results are suitable considered acceptable.

4.1. **Segmentation based on the image dataset.** Here we randomly select six gray images and seven color images from the Weizmann Institute of science images dataset to be the testing images as shown in Figure 1. The segmentation results are generated by above segmentation models shown in Figure 2 and 3. It is obvious to find that the CV and the DTC models have obvious under segmentation phenomenon such as the dendritic crack in segmented image '#1'. The GMAC can not separate dendritic terminals from the background when segmenting '#1'. To the models of the CV, the GMAC, the ICTM and the DTC models, they also have wrong boundaries and over segmentation phenomenon when segmenting '#4'. In addition, the details in lower right corner of the image '#5' can not be correctly segmented out by using the CV model. In addition, we also consider these models to segment the color images and it is obvious that we can obtain the similar conclusions as to segment the gray images from Figure 3.

| (a) #1 | (b) #2 | (c) #3 | (d) #4 | (e) #5 | (f) #6 |

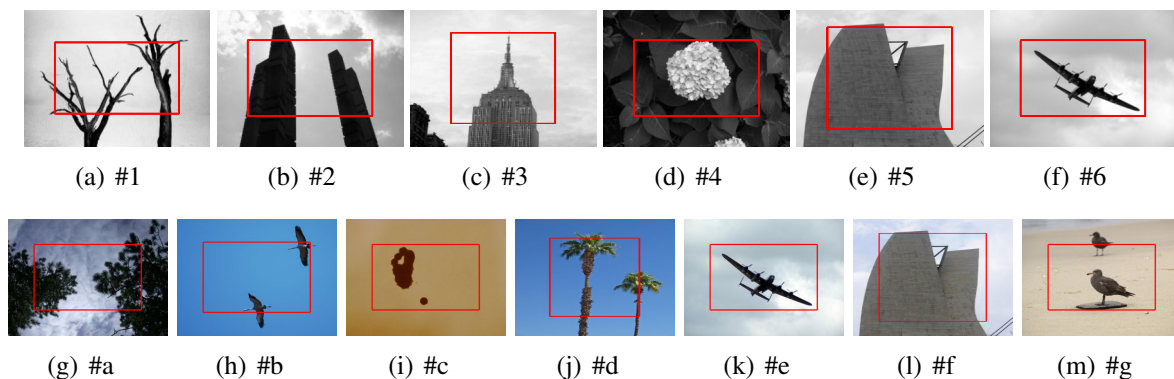| (g) #a | (h) #b | (i) #c | (j) #d | (k) #e | (l) #f | (m) #g |

FIGURE 1. Testing images from the Weizmann Institute of science images dataset and initial contours are plotted as the red boxes.

To evaluate the accuracy of the segmentation results, the related quantitative indexes as JS, SA, F1-score and κ are shown in Table 1 and Table 2. From these tables, we can observe that our proposed model has higher quantitative indexes. This means that our proposed model can segment the image more accurately. On the other hand, from the variance of Table 1 and Table 2, our proposed model has smaller variance than other models and then implies better robustness.

Besides contrast visual effect and quantitative indexes, we also compare the computation time among above models in the form of histograms for six gray natural images. It can be seen from Figure 4 that the WBHV model takes the longest CPU time and our proposed model takes the shortest CPU time. To sum up, our proposed model uses the least CPU time to obtain better image quality. Since the proposed method is a non-convex optimization problem, we do not give a theoretical analysis of the convergence of Algorithm 1. However, in order to explore whether the Algorithm 1 converges, we choose '#3' and '#4' in Figure 1 to be the testing images. Specifically, we respectively define some errors as bias error (called L_1), relative error

https://www.wisdom.weizmann.ac.il/~vision/Seg_Evaluation_DB/

TABLE 1.   The JS, SA, F1 and κ values on six gray images of the CV [19], GMAC [32], ICTM [30], WBHV [35], DTC [34], and OURS.

Criteria	JS						SA					
Images	CV	GMAC	ICTM	WBHV	DTC	OURS	CV	GMAC	ICTM	WBHV	DTC	OURS
#1	0.8349	0.8409	0.8351	0.8391	0.7656	0.8441	0.9765	0.9780	0.9772	0.9778	0.9668	0.9784
#2	0.9898	0.9936	0.9935	0.9932	0.9778	0.9938	0.9971	0.9982	0.9981	0.9981	0.9936	0.9982
#3	0.7827	0.9647	0.9643	0.9646	0.9406	0.9678	0.9575	0.9931	0.9930	0.9931	0.9883	0.9937
#4	0.8969	0.9527	0.9511	0.9598	0.9399	0.9677	0.9875	0.9942	0.9940	0.9951	0.9824	0.9961
#5	0.9760	0.9896	0.9893	0.9897	0.9621	0.9896	0.9865	0.9942	0.9940	0.9943	0.9860	0.9942
#6	0.7837	0.7763	0.7803	0.7861	0.7499	0.7866	0.9880	0.9875	0.9878	0.9881	0.9927	0.9881
Mean	0.8773	0.9196	0.9189	0.9221	0.8893	**0.9249**	0.9822	0.9909	0.9907	0.9911	0.9750	**0.9915**
Variance	0.0085	0.0081	0.0080	0.0077	0.0106	**0.0077**	0.0002	0.0001	0.0001	0.0001	0.0005	**0.0001**
Criteria	F1						κ					
Images	CV	GMAC	ICTM	WBHV	DTC	OURS	CV	GMAC	ICTM	WBHV	DTC	OURS
#1	0.9100	0.9136	0.9101	0.9125	0.8673	0.9155	0.8965	0.9010	0.8971	0.8998	0.8485	0.9031
#2	0.9949	0.9968	0.9967	0.9966	0.9888	0.9969	0.9928	0.9955	0.9955	0.9952	0.9843	0.9956
#3	0.8781	0.9820	0.9818	0.9820	0.9684	0.9836	0.8528	0.9778	0.9775	0.9777	0.9622	0.9797
#4	0.9456	0.9758	0.9749	0.9795	0.9807	0.9836	0.9386	0.9725	0.9715	0.9767	0.9646	0.9813
#5	0.9879	0.9948	0.9946	0.9948	0.8571	0.9948	0.9726	0.9882	0.9879	0.9884	0.8498	0.9883
#6	0.8787	0.8740	0.8766	0.8803	0.9690	0.8806	0.8725	0.8676	0.8702	0.8741	0.9649	0.8744
Mean	0.9325	0.9562	0.9558	0.9576	0.9396	**0.9592**	0.9210	0.9504	0.9500	0.9520	0.9291	**0.9537**
Variance	0.0027	0.0026	0.0025	0.0024	0.0037	**0.0024**	0.0032	0.0028	0.0028	0.0027	0.0039	**0.0027**

TABLE 2.   The JS, SA, F1 and κ values on seven color images of the CV [19], GMAC [32], ICTM [30], WBHV [35], DTC [34], and OURS.

| Criteria	JS						SA					
Images	CV	GMAC	ICTM	WBHV	DTC	OURS	CV	GMAC	ICTM	WBHV	DTC	OURS
#a	0.8971	0.9002	0.9112	0.9112	0.7819	0.9149	0.9496	0.9510	0.9565	0.9564	0.9879	0.9580
#b	0.8705	0.8501	0.8595	0.8627	0.9194	0.8780	0.9956	0.9949	0.9952	0.9953	0.9965	0.9958
#c	0.9264	0.9180	0.9177	0.9204	0.8431	0.9306	0.9968	0.9965	0.9965	0.9966	0.9796	0.9970
#d	0.8474	0.7834	0.8358	0.8235	0.6092	0.8741	0.9797	0.9729	0.9793	0.9776	0.6207	0.9836
#e	0.8219	0.7837	0.7837	0.7840	0.7506	0.8510	0.9901	0.9880	0.9880	0.9880	0.9855	0.9917
#f	0.9897	0.9901	0.9900	0.9901	0.9897	0.9907	0.9943	0.9945	0.9944	0.9945	0.9942	0.9948
#g	0.7236	0.7480	0.7497	0.7504	0.6285	0.7512	0.9831	0.9853	0.9855	0.9855	0.7980	0.9852
Mean	0.8681	0.8534	0.8639	0.8632	0.7089	**0.8844**	0.9842	0.9833	0.9851	0.9848	0.9089	**0.9866**
Variance	0.0071	0.0077	0.0069	0.0070	0.0200	**0.0056**	0.0003	0.0003	0.0002	0.0002	0.0212	**0.0002**
Criteria	F1						κ					
Images	CV	GMAC	ICTM	WBHV	DTC	OURS	CV	GMAC	ICTM	WBHV	DTC	OURS
#a	0.9458	0.9475	0.9536	0.9535	0.8776	0.9555	0.8989	0.9017	0.9128	0.9125	0.8713	0.9159
#b	0.9307	0.9190	0.9244	0.9263	0.9580	0.9350	0.9285	0.9164	0.9220	0.9239	0.9562	0.9329
#c	0.9618	0.9573	0.9571	0.9586	0.9149	0.9640	0.9602	0.9554	0.9553	0.9568	0.9033	0.9625
#d	0.9174	0.8785	0.9106	0.9032	0.7571	0.9328	0.9058	0.8635	0.8989	0.8906	0.6045	0.9235
#e	0.9022	0.8787	0.8787	0.8789	0.8575	0.9195	0.8971	0.8725	0.8725	0.8727	0.8499	0.9151
#f	0.9948	0.9950	0.9950	0.9950	0.9948	0.9953	0.9884	0.9889	0.9887	0.9888	0.9983	0.9895
#g	0.8397	0.8559	0.8570	0.8574	0.7719	0.8579	0.8308	0.8481	0.8494	0.8498	0.9560	0.8501
Mean	0.9275	0.9188	0.9252	0.9247	0.8760	**0.9371**	0.9157	0.9066	0.9142	0.9136	0.8272	**0.9271**
Variance	0.0024	0.0026	0.0023	0.0023	0.0079	**0.0018**	0.0026	0.0026	0.0023	0.0023	0.0254	**0.0020**
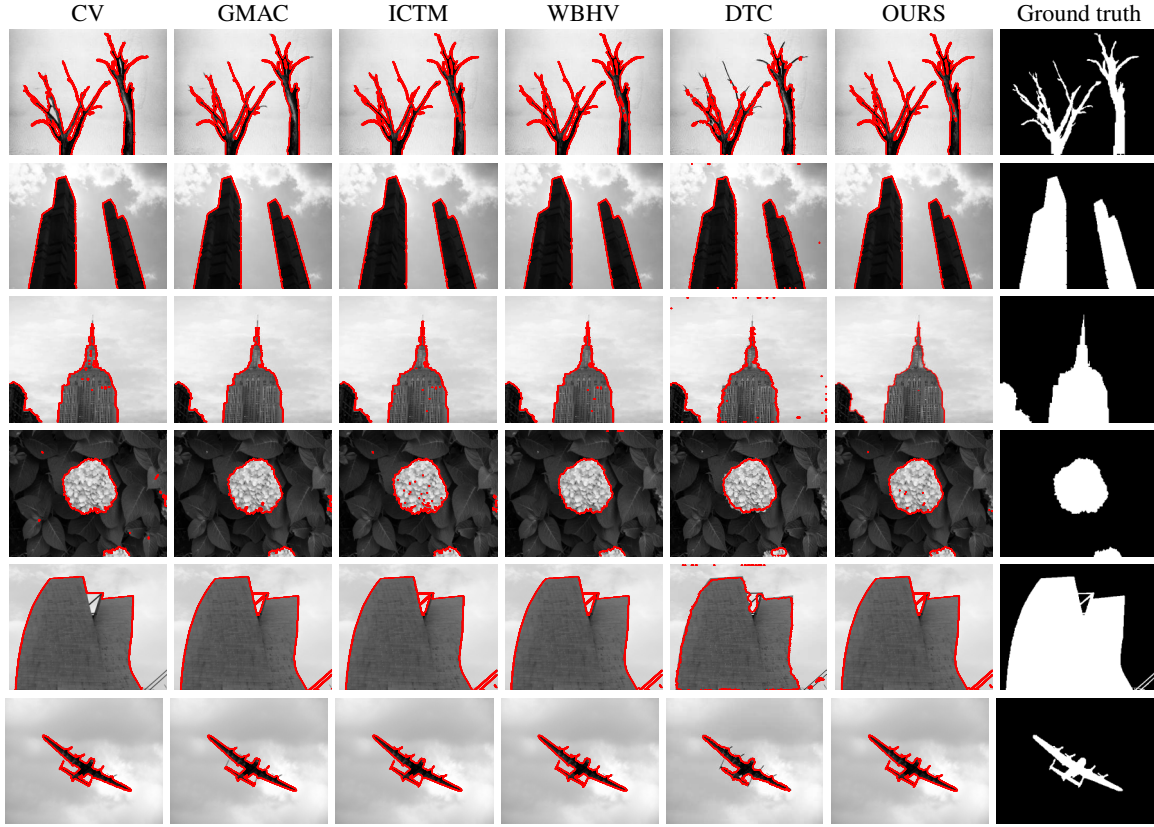
FIGURE 2. Segmentation comparison on gray images. Top six colums: segmentation results of the CV [19], GMAC [32], ICTM [30], WBHV [35], DTC [34] and OURS, respectively. The last column: ground truth. The experiment parameters: (1; 0.125, 1; 0.003, 0.01; 14, 15; 0.8, 0.4; 16), (1; 1, 0.125; 0.003, 0.01; 15, 10; 0.8, 0.5; 25), (1; 0.13, 1; 0.005, 0.01; 10, 10; 2, 1; 7), (1; 0.125, 1; 0.006, 0.01; 2, 10; 1.6, 0.5; 5), (1; 0.13, 2; 0.006, 0.01; 25, 10; 1.6, 0.5; 45), (1; 0.125, 1; 0.007, 0.01; 25, 10; 2, 10; 400).

of Lagrange multiplier (called L_1), and the variable error (called RE) in the following

$$R_1 = \left\| \mathbf{z}^k - \nabla^2 u^k \right\|_1, \ \ L_1 = \frac{\left\| \boldsymbol{\eta}^k - \boldsymbol{\eta}^{k-1} \right\|_1}{\left\| \boldsymbol{\eta}^{k-1} \right\|_1} \ \text{ and } \ RE = \frac{\left\| u^k - u^{k-1} \right\|_1}{\left\| u^{k-1} \right\|_1}.$$

It is easy to observe the convergence of the error curves against the iteration and then these facts illustrate the reasonability and the stability of our proposed numerical algorithm.

4.2. **Segmentation based on the noisy images.** Here we consider the impact of noise on the segmentation result and the testing images are shown in the first row of Figure 6. To this end, we add the white Gaussian noise with the deviation $\sigma = 0.05, 0.15$ and the salt & pepper noise with density of 5% and 15% to images '#A' and '#B', respectively. The initial contours of the segmentation models are shown as the rectangular box in the second row. The last six rows are the corresponding segmentation results generated by aforementioned models. The results show that the GMAC, the WBHV and the DTC rarely mistake noise as boundary, but in the CV and the ICTM, the noise near the boundary is mistakenly divided into boundaries.
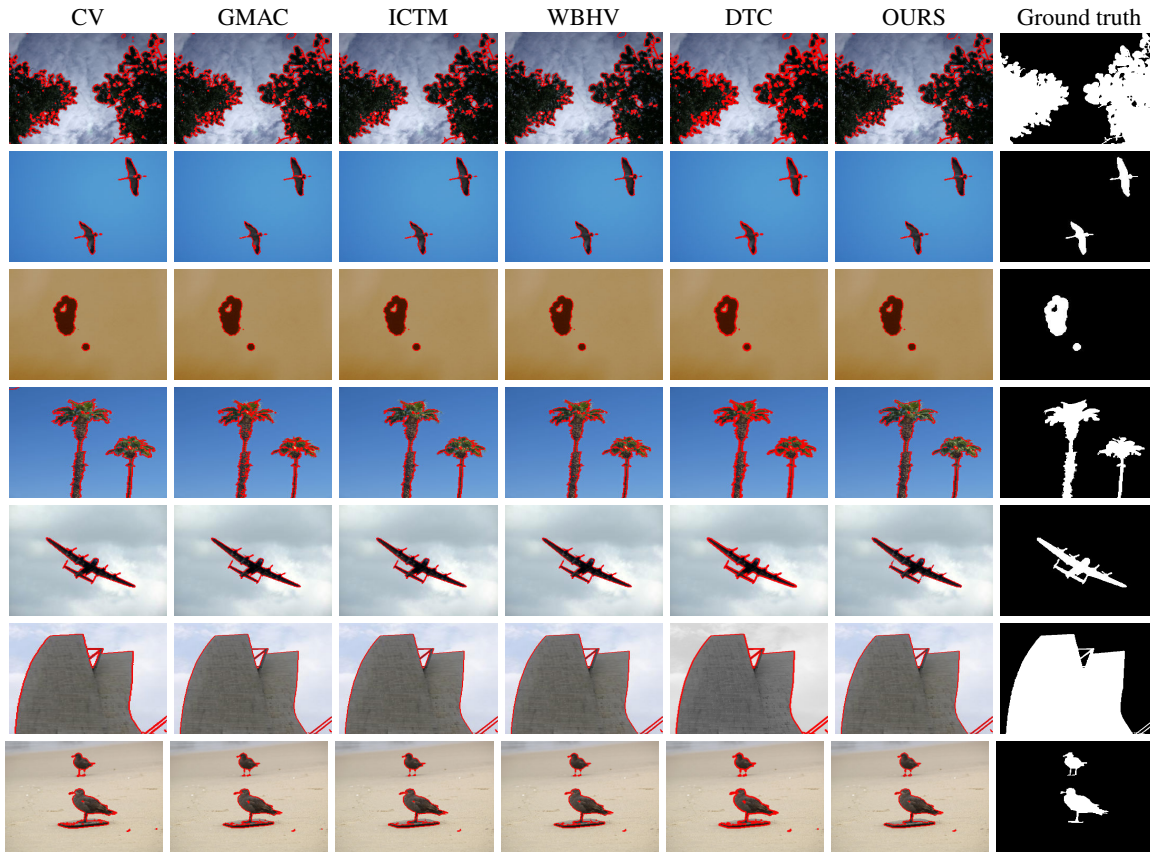
FIGURE 3. Segmentation comparison on seven color images. Top six columns: segmentation results of the CV [19], GMAC [32], ICTM [30], WBHV [35], DTC [34], and OURS, respectively. The last column: ground truth. The experiment parameters: (1; 0.1, 1; 0.01, 0.01; 3, 10; 1, 1; 45), (2; 0.125, 1; 0.001, 0.01; 45, 1; 5, 0.01; 23), (1; 0.125, 1; 0.02, 0.01; 46, 10; 5, 1; 8), (1; 0.1, 1; 0.05, 0.02; 45, 1; 10, 0.01; 8), (2; 0.125, 2; 0.002, 0.01; 150, 1; 5, 0.5; 2), (1; 0.13, 1; 0.001, 0.01; 10, 1; 5, 0.5; 35), (1; 0.125, 1; 0.008, 0.01; 45, 1; 5, 0.5; 19).
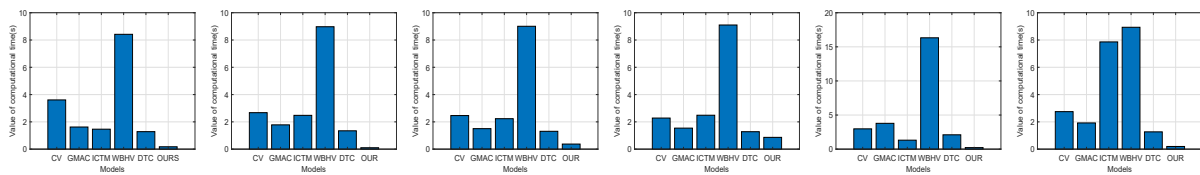
FIGURE 4. Compare the CPU times of different models (CV [19], GMAC [32], ICTM [30], WBHV [35], DTC [34], and OURS) on six gray images.

While segmenting high-intensity noisy images, the GMAC, the WBHV and the DTC fail to segment the upper left vertical line in '#A'. At the same time, the right boundary of 'U-shaped' target in '#B' is incomplete and fractured. In contrast to the segmentation results generated by other compared models, our proposed model is more robust against the noise effect and the segmentation boundary is relatively continuous.
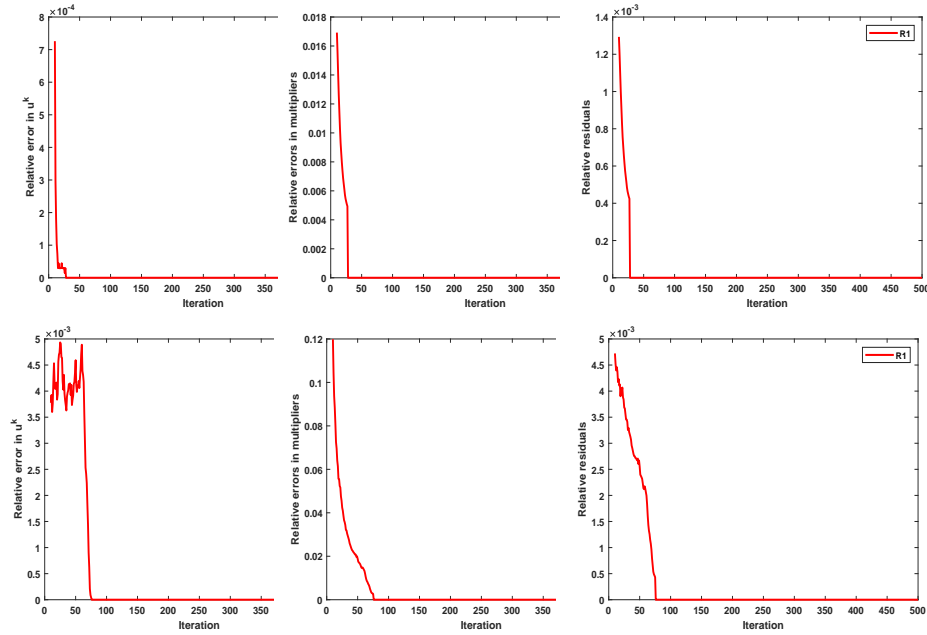
FIGURE 5. The plots of relative errors from the first column to the third column as RE, L_1, and R_1 against the iteration by using Algorithm 1 to segment images '#3' and '#4'.

Besides the visual results, the evaluation index values are arranged in Figure 7. It is obvious that four indicators of our model in the two images are the highest, indicating that our model outperforms other models for segmenting the noisy images.

4.3. **Initial contour influence on ultrasonic images.** In order to further demonstrate the effectiveness of our proposed model, some ultrasonic images come from Department of Ultrasound in Henan Provincial People's Hospital are considered. These images have approved by the Medical Ethics Committee of Henan Provincial People's Hospital. The first column of Figure 9 is the original images and the corresponding initial contours. In order to verify the influence of initial contours on the models, we consider three different initial contours. The segmentation results are shown in the last six columns of Figure 9. It is easy to observe that the CV and the GMAC depend on the original contour more than other models. As a contrast, we also find that the segmentation result of our proposed model is better than other models. Especially, the WBHV has some wrong segmentation on the left side. In conclusion, our proposed model is more robust to the selection of initial contour and the segmentation result is more accurate. These observations still illustrate the effectiveness of our proposed model again.

4.4. **Effect of the weighted functions $\alpha(f)$ and $\beta(f)$.** It is well known that the convolution operator used in the heat kernel convolution can blur the image edge. In order to explain the reasonability of the weighted functions to overcome this drawback, we choose '#3' in Figure 1 as the testing image, where this image includes some details such spire and edges. In this experimentation, we respectively set $\alpha(f)$ and $\beta(f)$ to be different setting in the proposed model (3.1). For example, if we set $\beta(f) = 0$, then the model is degraded into the weighted CV model [32]. In addition, if we set $\beta(f) = 1$ and $\beta(f) = 1$, the model is degraded into the classical MS model

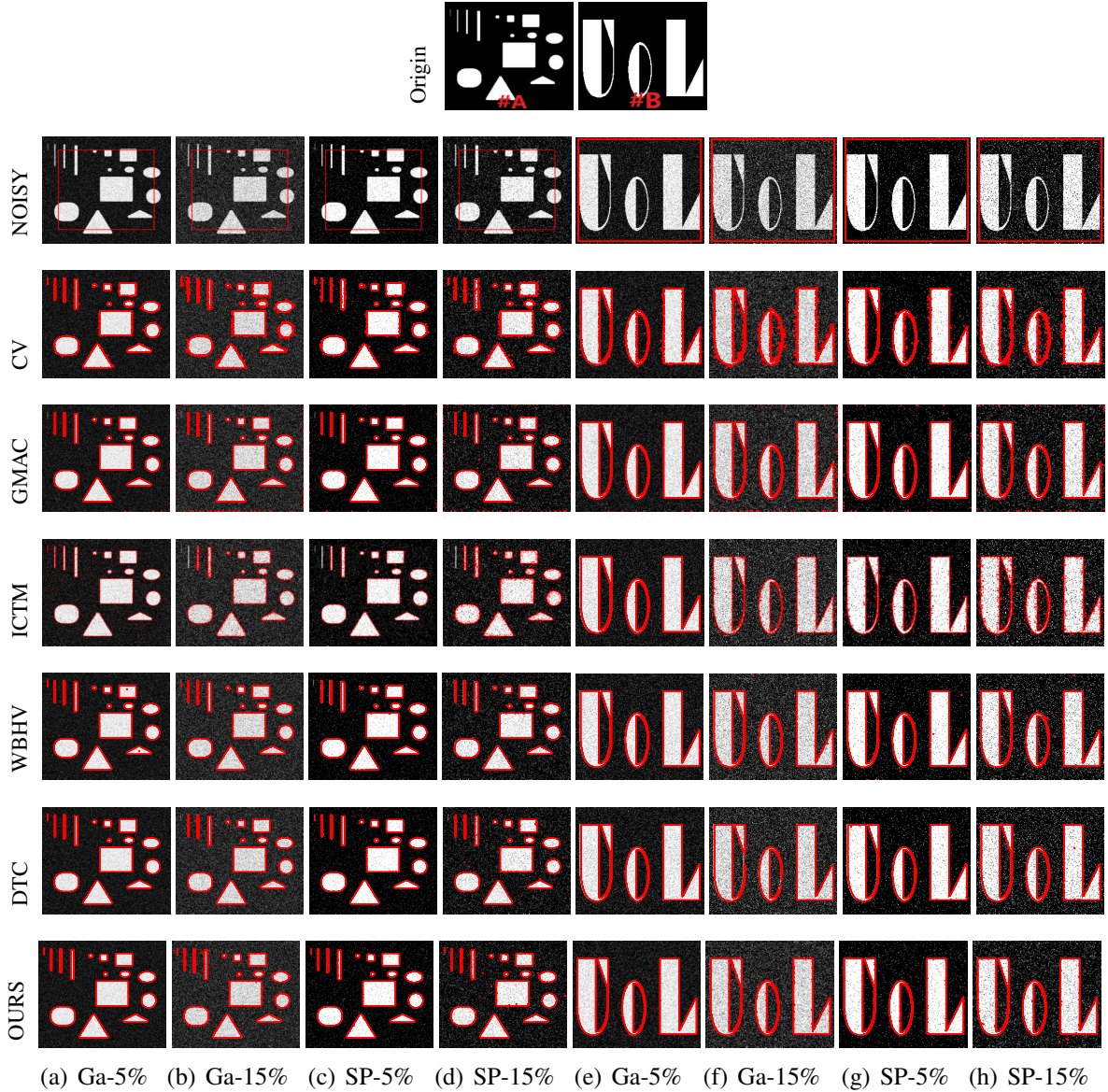(a) Ga-5% (b) Ga-15% (c) SP-5% (d) SP-15% (e) Ga-5% (f) Ga-15% (g) SP-5% (h) SP-15%

FIGURE 6. Segmentation comparison on two Synthetic images with difference noise level. The first row: original images. Images with White Gaussian (Ga) noise of $\sigma = 0.05$ and $\sigma = 0.15$ are shown in the (b) and (f) columns; Images with Salt and Pepper noise of 5% and 15% are shown in the (d) and (h) columns.

[36]. To the segmentation images, we can observe some over-segmentation phenomenons in the area marked by green box when $\alpha(f) = 0$ or $\beta(f) = 0, 1$ and under-segmentation phenomenons when $\alpha(f) = 1$ or $\alpha(f) = \beta(f) = 1$ in Figure 8. As a contrast, our proposed method can efficiently segment these details.

5. CONCLUSION

In this work, we proposed an efficient numerical method to solve a weighted type segmentation model. To the proposed method, the weighted functions were used to describe the details of
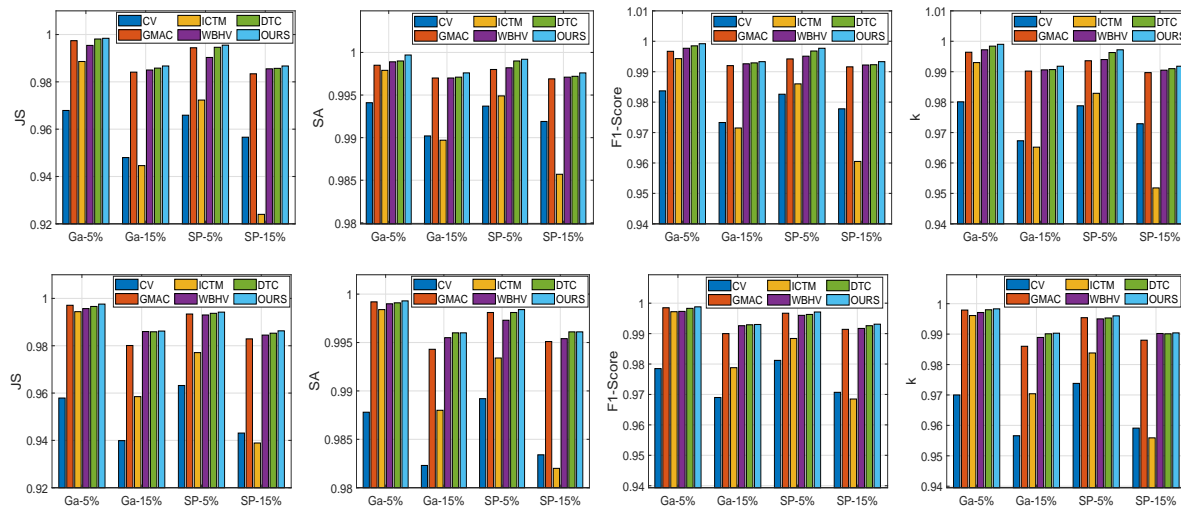
FIGURE 7. Statistical results (JS, SA, F1-Score, and κ) for images '#A' and '#B' with different noise. The first row: four evaluation indicators for different models in '#A'. The second row: four evaluation indicators for different models in '#B'.
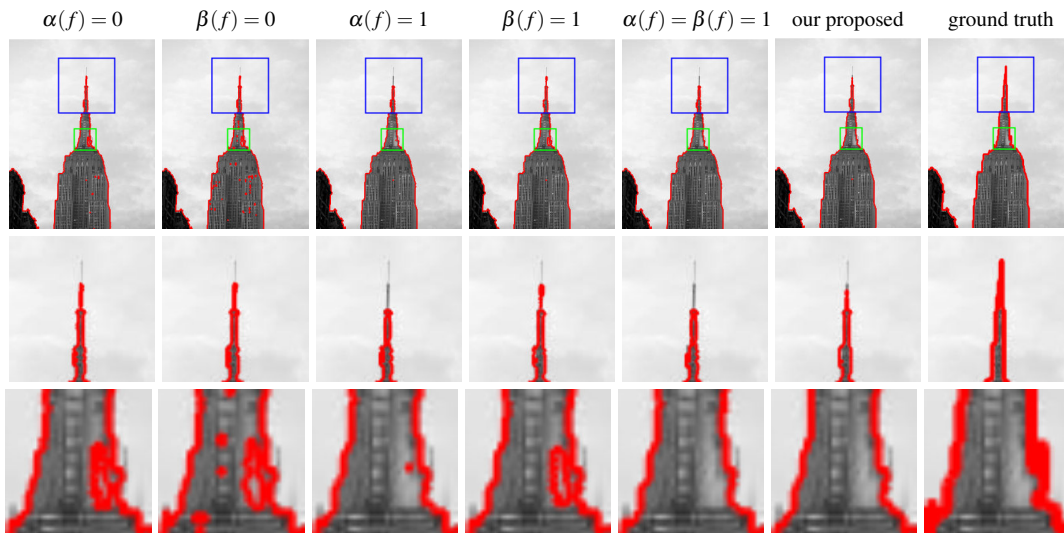

FIGURE 8. Spatially adaptive weights $\alpha(f)$ and $\beta(f)$ of the image '#3' in the proposed model (3.1). Visual difference is marked by the blue box and the green box.

the image edge. In order to reduce the difficulty of numerical method, we first use the heat kernel convolution to approximatively replace the total variation term and then used the ADMM to split this approximated problem into several easily solvable subproblems. We performed several experiments with real and synthetic images for the validation of the proposed method. Moreover, we adapted the segmentation accuracy (SA), F1-Score (F1), κ-coefficient (κ), and Jaccard Similarity (JS) for the quantitative validation of our method. Results demonstrate that the proposed procedure has accomplished improved results that stood out from several state-of-the-art segmentation models.
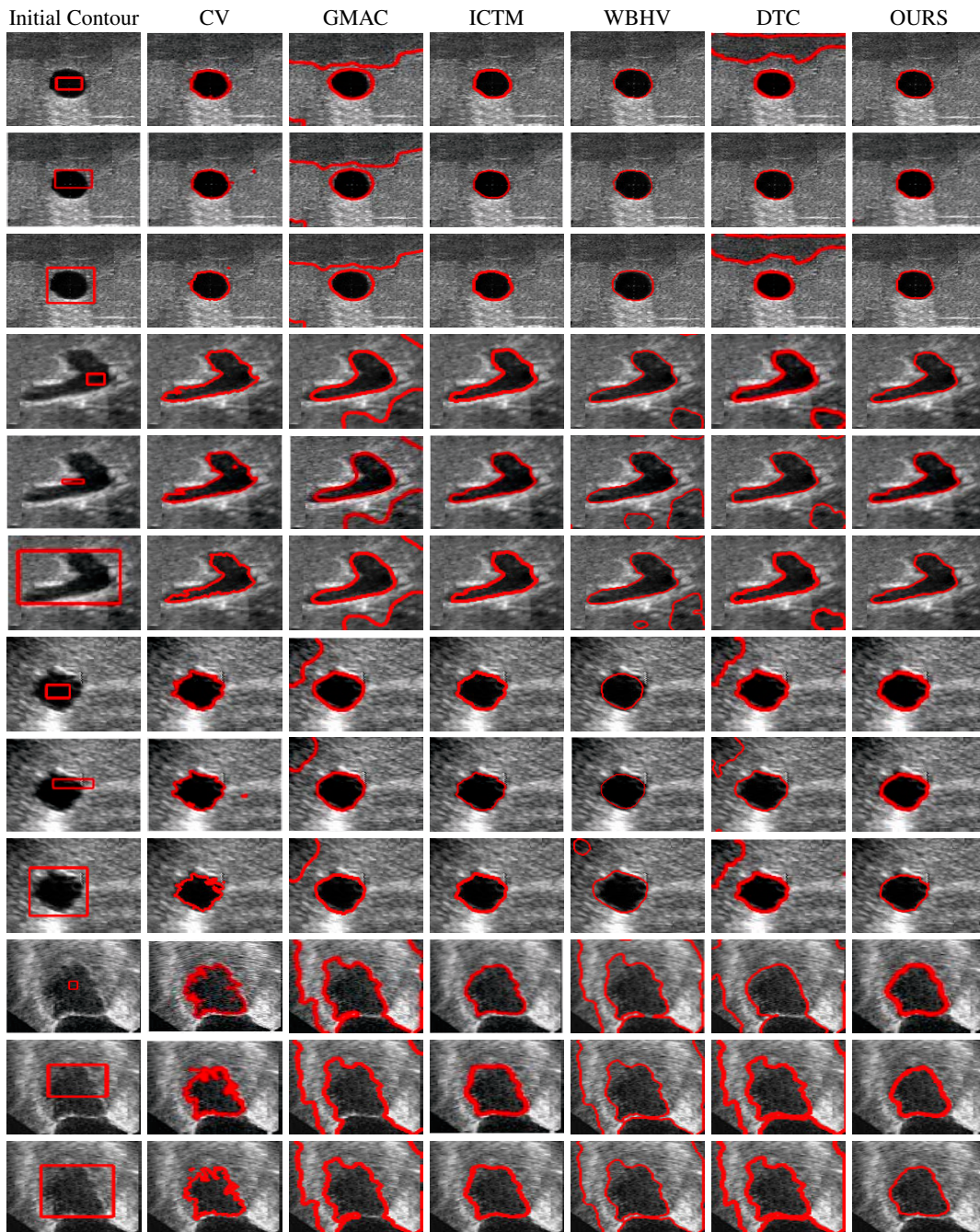
FIGURE 9. Segmentation results of the ultrasonic images under different initial contours. The first column is the input images and the initial contours. The latter six columns are the segmentation results for the CV [19], GMAC [32], ICTM [30], WBHV [35], DTC [34], and OURS, respectively.

Acknowledgements

REFERENCES

[1] H. Li, H. Luo, W. Huan, Z. Shi, C. Yan, La. Wang, Y. Mu, Y. Liu, Automatic lumbar spinal MRI image segmentation with a multi-scale attention network, Neural Computing and Applications, 33 (2021), 11589-11602.

[2] Y. Liu, Q. Zhu, F. Cao, J. Chen, G. Lu, High-resolution remote sensing image segmentation framework based on attention mechanism and adaptive weighting, International Journal of Geo-Information, 10 (2021), 1-18.

[3] C. Moore, S He, Q Zheng, J. Mordkoff, Target-flanker similarity effects reflect image segmentation not perceptual grouping, Attention, Perception, Psychophysics, 83 (2021), 658-675.

[4] C. Xu, Y. Chen, C. Xu, End-to-end dilated convolution network for document image semantic segmentation, Journal of Central South University, 28 (2021), 1765-1774.

[5] Y. Xia, S. Eberl, L. Wen, M. Fulham, D. Feng, Dual-modality brain PET-CT image segmentation based on adaptive use of functional and anatomical information, Computerized Medical Imaging and Graphics, 36 (2012), 47-53.

[6] P. Azimpour, T. Bahraini, H. Yazdi. Hyperspectral image denoising via clustering-based latent variable in variational bayesian framework, IEEE Transactions on Geoscience and Remote Sensing, 59 (2021), 3266-3276.

[7] Y. Wu, P. Qian, X. Zhang, Two-level wavelet-based convolutional neural network for image deblurring, IEEE Access, 9 (2021), 45853-45863.

[8] Y. Xu, Z. Li, X. Zhang, et al. Low-dose PET image denoising based on coupled dictionary learning. Nuclear Instruments and Methods in Physics Research Section A: Accelerators, Spectrometers, Detectors and Associated Equipment, 1020 (2021), 165908.

[9] Y. Zhu, X. Pan, T. Lv, Y. Liu, L. Li, DESN: An unsupervised MR image denoising network with deep image prior, Theoretical Computer Science, 880 (2021), 97-110.

[10] M. Gou, Y. Rao, M. Zhang, J Sun, K. Cheng, Automatic image annotation and deep learning for tooth CT image segmentation, International Conference on Image and Graphics, pp. 519-528, 2019.

[11] Q. Lin, X. Chen, C. Chen, J. M. Garibaldi, Fuzzy DCNN: incorporating fuzzy integral layers to deep convolutional neural networks for image segmentation, IEEE International Conference on Fuzzy Systems, pp. 1-7, 2021.

[12] M. Lin, Q. Cai, J. Zhou, 3D Md-Unet: A novel model of multi-dataset collaboration for medical image segmentation, Neurocomputing, 492 (2022), 530-544.

[13] L. Chen, G. Papandreou, I. Kokkinos, K. Murphy, A. Yuille, DeepLab: Semantic image segmentation with deep convolutional nets, atrous convolution, and fully connected CRFs. IEEE Transactions on Pattern Analysis and Machine Intelligence, 40 (2018), 834-848.

[14] H. Park, T. Schoepflin, Y. Kim. Active contour model with gradient directional information: Directional snake, IEEE Transactions on Circuits and Systems for Video Technology, 11 (2001), 252-256.

[15] M. Falcone, G. Paolucci, S. Tozza, A high-order scheme for image segmentation via a modified level-set method, SIAM Journal on Imaging Sciences, 13 (2020), 497-534.

[16] J. Zhu, Y. Zeng, H. Xu, J. Li, S. Tian, H. Liu. Maximum a posterior based level set approach for image segmentation with intensity inhomogeneity, Signal Processing, 181 (2021), 107896.

[17] H. Wang, Y. Du, J. Han. An integrated two-stage approach for image segmentation via active contours, Multimedia Tools and Applications, 79 (2020), 21177-21195.

[18] M. Abdel-Basset, V. Chang, R. Mohamed. A novel equilibrium optimization algorithm for multi-thresholding image segmentation problems, Neural Computing and Applications, 33 (2020), 10685-10718.

[19] T. Chan, L. Vese. Active contours without edges, IEEE Transactions on Image Processing, 10 (2001), 266-277.

[20] T. Chan, S. Esedoglu, M. Nikolova, Algorithms for finding global minimizers of image segmentation and denoising models, SIAM Journal on Applied Mathematics, 66 (2006), 1632-1648.

[21] A. Chambolle, D. Cremers, T. Pock, A convex relaxation approach for computing minimal partitions, IEEE Computer Society Conference on Computer Vision, pp. 810-817, 2008.

[22] J. Yuan, E. Bae, X. C. Tai, A study on continuous max-flow and min-cut approaches, The Twenty-Third IEEE Conference on Computer Vision, pp. 2217-2224, 2010.

[23] C. Li, C. Y. Kao, J. C. Gore, Z. Ding. Minimization of region-scalable fitting energy for image segmentation, IEEE Transactions on Image Processing, 17 (2008), 1940-1949.

[24] X. Wang, D. Huang, H. Xu. An efficient local Chan-Vese model for image segmentation, Pattern Recognition, 43 (2010), 603-618.

[25] K. Zhang, L. Zhang, K. Lam, D. Zhang. A level set approach to image segmentation with intensity inhomogeneity, IEEE Transactions on cybernetics, 46 (2015), 546-557.

[26] J. Wang, L. Ju, X. Wang, An edge-weighted centroidal Voronoi tessellation model for image segmentation, IEEE Transactions on Image Processing, 18 (2009), 1844-1858.

[27] Y. Cao, L. Ju, Y. Zhou, S. Wang, 3D superalloy grain segmentation using a multichannel edge-weighted centroidal voronoi tessellation algorithm, IEEE Transactions on Image Processing, 22 (2013), 4123-4135.

[28] B. Merriman, J. Bence, S. Osher, Motion of multiple junctions: A level set approach, Journal of Computational Physics, 112 (1994), 334-363.

[29] S. Esedoglu, F. Otto, Threshold dynamics for networks with arbitrary surface tensions, Communications on Pure and Applied Mathematics, 68 (2015), 808-864.

[30] D. Wang, H. Li, X. Wei, X. Wang, An efficient iterative thresholding method for image segmentation, Journal of Computational Physics, 350 (2017), 657-667.

[31] D. Mumford, J. Shah, Optimal approximations by piecewise smooth functions and associated variational problems, Communications on Pure Applied Mathematics, 42 (1989), 577-685.

[32] X. Bresson, S. Esedoglu, P. Vandergheynst, J. Thiran, S. Osher, Fast global minimization of the active contour/snake model, Journal of Mathematical Imaging and Vision, 28 (2007), 151-167.

[33] D. Wang, X. Wang, The iterative convolution-thresholding method (ICTM) for image segmentation, Pattern Recognition, 130 (2022), 108794.

[34] Q. Zhong, Y. Li, Y. Yang, Y. Duan, Minimizing discrete total curvature for image processing, IEEE/CVF Conference on Computer Vision and Pattern Recognition, pp. 9471-9479, 2020.

[35] Y. Yang, Q. Zhong, Y. Duan, T. Zeng, A weighted bounded Hessian variational model for image labeling and segmentation, Signal Processing, 173 (2020), 107564.

[36] R. Chan, T. Zeng, X. Cai, A two-stage image segmentation method using a convex variant of the Mumford–Shah model and thresholding, SIAM Journal on Imaging Sciences, 6 (2013), 368-390.